# Regional Perturbations in a Global Background Model of Glacial Isostasy

H.H.A. Schotman, P. Wu, L.L.A. Vermeersen

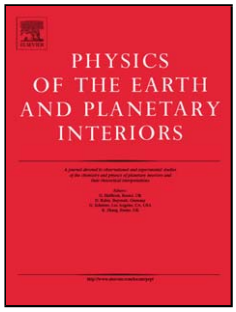


Title: Regional Perturbations in a Global Background Model of Glacial Isostasy

Authors: H.H.A. Schotman, P. Wu, L.L.A. Vermeersen

PII: S0031-9201(08)00037-X
DOI: doi:10.1016/j.pepi.2008.02.010
Reference: PEPI 4905

To appear in: *Physics of the Earth and Planetary Interiors*

Received date: 29-10-2007
Revised date: 17-2-2008
Accepted date: 26-2-2008

Please cite this article as: Schotman, H.H.A., Wu, P., Vermeersen, L.L.A., Regional Perturbations in a Global Background Model of Glacial Isostasy, *Physics of the Earth and Planetary Interiors* (2007), doi:10.1016/j.pepi.2008.02.010

# Regional Perturbations in a Global Background Model of Glacial Isostasy

H.H.A. Schotman [a,c] P. Wu [b] L.L.A. Vermeersen [c,*]

[a] *SRON Netherlands Institute for Space Research, Sorbonnelaan 2, 3584 CA Utrecht, The Netherlands*

[b] *Department of Geoscience, University of Calgary, 2500 University Drive NW., Alberta, Canada T2N-1N4*

[c] *DEOS, Astrodynamics and Satellite Systems, Faculty of Aerospace Engineering, Delft University of Technology, Kluyverweg 1, 2629 HS Delft, The Netherlands*

**Abstract**

In Schotman and Vermeersen (2005, Earth Planet. Sci. Lett. 236), the effect of crustal and asthenospheric low-viscosity zones (LVZs) on geoid heights was shown, as predicted by models of glacial-isostatic adjustment (GIA). The governing equations were solved analytically in the spectral domain, which makes the method used accurate and fast. However, it does not allow for (large) lateral variations in earth stratification. As the properties of shallow LVZs can be expected to vary laterally, we have developed a finite-element model based on ABAQUS. Global (spherical-3D) finite-element models are currently not capable of providing high-resolution predictions, which we expect due to the shallowness of the LVZs. We therefore use a regional (flat-3D) model and compute geoid heights from the predicted displacements at density boundaries by solving Laplace's equation in the Fourier-transformed domain. The finite-element model is not self-gravitating, but we compare the results

with a self-gravitating spectral model under the assumption that the lack of self-gravitation is partly compensated by the lack of sphericity, and that long-wavelength differences largely cancel out when using perturbations, which are the difference between a model with and without an LVZ. We show that geoid height perturbations due to an LVZ can be computed accurately, though the accuracy deteriorates somewhat with the depth of the LVZ. Moreover, we show that horizontal rates of displacement, though not accurate for total displacements, are accurate for perturbations in the near field. We show the effect of lateral variations in the properties of the LVZ and in lithospheric thickness, and compute geoid height perturbations for Northern Europe based on a simple laterally heterogeneous model. The model is forced with a realistic ice-load history and a eustatic ocean-load history. The errors introduced by using a eustatic ocean-load history instead of realistic oceans are generally smaller than 10%, but might be critical for perturbations due to crustal LVZs.

*Key words:* glacial isostasy, satellite gravity, GPS measurements, finite-element modeling, rheology of the crust and upper mantle, halfspace modeling

*PACS:* 91.10.Fc, 91.10.Kg, 91.10.Op, 91.10.Vr, 91.32.De, 91.32.Gh

## 1 Introduction

The process of glacial-isostatic adjustment (GIA), in which the solid earth is deformed by load changes due to variations in the volume of continental ice sheets, is commonly associated with long-wavelength phenomena (spherical harmonic degree $< 20$) as land-uplift in Scandinavia ("postglacial rebound", e.g. Milne et al., 2001), part of the geoid low in Hudson Bay-area (e.g. Tamisiea

* Corresponding author
*Email address:* l.l.a.vermeersen@tudelft.nl (L.L.A. Vermeersen).

et al., 2007), and variations in the position and speed of the earth's axis of rotation (polar wander and changes in length-of-day, e.g. Mitrovica et al., 2005). These phenomena are mainly influenced by the thickness of the lithosphere and the viscosity of the mantle, and can to a large extent be explained using spherical, radially stratified (*laterally homogeneous* or 1D) viscoelastic earth models, which often use a spherical harmonic expansion to solve the governing equations in the spectral (SP) domain. In the case of lateral variations, the transformed differential equations in SP methods can no longer be solved separately for each degree due to mode coupling (Wu, 2002), which complicates the use of the SP method, especially for large viscosity gradients. Recently, *laterally heterogeneous* (3D) spherical earth models based on the finite-element (FE) method have been developed, showing the effect of lateral variations in lithospheric thickness and mantle viscosity (Wu and van der Wal, 2003; Zhong et al., 2003; Wu et al., 2005; Latychev et al., 2005).

The upcoming GOCE satellite gravity mission, planned for launch by ESA on May 15 2008, is predicted to measure the static gravity field with centimeter accuracy at a resolution of 100 km or less (Visser et al., 2002). This makes the detection of *high-resolution* signals as expected from shallow earth structures possible. In GIA, high-harmonic signatures (spherical harmonic degree $> 20$) can be induced by shallow layers (depth $< 200$ km) with low viscosity ($\sim 10^{18} - 10^{20}$ Pas, Schotman and Vermeersen, 2005). Crustal low-viscosity zones (CLVZs) are layers in the lower crust which have viscosities that are significantly smaller than the high-viscosity, for GIA studies effectively elastic, upper crust and lithospheric mantle. As the presence and properties of CLVZs depend strongly on thermal regime (Meissner and Kusznir, 1987; Ranalli and Murphy, 1987; Watts and Burov, 2003), these can in principle not be modeled

using 1D-stratified earth models. In Northern Europe for example, CLVZs are not expected in the cold and thick crust of the Baltic Shield, but might be present in surrounding younger continental shelves (Schotman and Vermeersen, 2005). Asthenospheric LVZs (ALVZs) can probably be found below the oceanic lithosphere and perhaps also below the continental shelves, but not below the Baltic Shield (Schotman and Vermeersen, 2005; Steffen and Kaufmann, 2005).

As these shallow low-viscosity layers induce high-resolution signals, the use of a 3D-spherical FE model is considered to be not feasible yet. We therefore test if predictions from a 3D-flat FE model, based on the commercial package ABAQUS (Wu, 2004), are accurate enough for computing geoid height *perturbations*. Perturbations are differences between predictions from a *perturbed* background model and predictions from the background model itself. Here we assume that we know the background model, consisting of a laterally homogeneous *earth stratification* and *ice-load history*, from previous GIA studies. As we concentrate on Northern Europe, this background model will be mainly based on Fennoscandian studies (Lambeck et al., 1998; Milne et al., 2001). The presence and properties of LVZs are, via thermal regime, closely related to the thickness of lithosphere. We are therefore also interested in constraining both properties of LVZs and the thickness of the lithosphere simultaneously. As an additional constraint, apart from high-resolution satellite-gravity data, we will consider the use of 3D-velocities as for example measured by the BIFROST network (Milne et al., 2001), which has an accuracy of 0.8-1.3 mm/yr in the vertical direction and 0.2-0.4 mm/yr in the horizontal direction (Johansson et al., 2002).

A change in the volume of continental ice sheets leads to a global change in

relative sea level (RSL), which is defined as the difference between a change in the ocean bottom topography and in the equipotential surface that coincides with mean sea level, the geoid. This makes GIA essentially a global process. In this global process, mass is conserved and redistributed gravitationally self-consistently, i.e. the mass redistribution on the surface and in the interior of the earth affect the gravitational potential, which in turn affects the mass redistribution. This is called *self-gravitation* and leads for example to a higher than *eustatic* (= uniformly distributed ice-mass equivalent) RSL near an ice sheet, because the mass of the ice sheet attracts the nearby ocean. Another effect is the long-wavelength effect in the solid earth: If we place an ice mass on the North Pole, not only the top of the earth will depress, but also the opposite side. This can be understood by considering the northward movement of the center of mass due to accumulation of mass at the North Pole, the subsequent flattening of the North Pole due to outward movement of the solid earth and the resulting change in gravitational potential. Both effects are illustrated in Figure **1** for an elliptical ice load, with a height at the center of 2500 m and a radius of 8°, which is on the North Pole for 10 kyrs.

In Section 6 we will test if we can use a eustatic ocean-load history to force the flat, non-self-gravitating FE model. The reason we do not want to include self-gravitation in the flat model is that we then have to iterate several times over a glacial cycle (see Section 2, and Wu (2004) for a spherical model), which is very demanding in terms of CPU time. We assume that we can neglect self-gravitation in the solid earth, because in a flat model the lack of self-gravitation is partly compensated by the lack of sphericity (Amelung and Wolf, 1994) and because we assume that some long-wavelength phenomena largely cancel out when using perturbations. Using an axisymmetric Heavi-

side load, we test in Section 4 the accuracy of predictions from the FE model by comparing differences with a spherical, self-gravitating SP model with the expected accuracies of the GOCE mission and the realized accuracy of the BIFROST network. Using the RSES ice-load history (Lambeck et al., 1998) and a simple model of Northern Europe, with CLVZs in relatively young continental crust and ALVZs below young continental and oceanic areas, we try to deduce in Section 5 if it is important to consider lateral heterogeneities in LVZs. We start with a short description of the theory, especially how we compute geoid heights from the output of the flat FE model (Section 2), followed by a description of the FE and SP model used in this study (Section 3).

## 2 Theory

The linearized, *elastic* equation of motion for geophysical problems in which inertia can be neglected is (e.g. Wu, 2004; Sabadini and Vermeersen, 2004, p. 5):

$$\vec{\nabla} \cdot \vec{\vec{\sigma}}_\delta - \vec{\nabla}(\vec{u} \cdot \rho_0 g_0 \vec{e}_r) - \rho_\delta g_0 \vec{e}_r - \rho_0 \vec{\nabla}\phi_\delta = 0 \tag{1}$$

with $\vec{\vec{\sigma}}$ the stress tensor, $\vec{u}$ the displacement vector, $\rho$ the density, $g$ the gravity acceleration, $\phi$ the gravity potential, and where the subscripts ('0', '$\delta$') denote the *initial* and *incremental* state (Wolf, 1998), respectively. For an *incompressible* material (Poisson's ratio $\nu = 0.5$), $\rho_\delta = 0$ and the third term (*internal buoyancy* due to material compressibility) vanishes. In this case, the gravity potential $\phi_\delta$ can be found from Laplace's equation:

$$\vec{\nabla}\phi_\delta = 0 \tag{2}$$

The *viscoelastic* problem, mostly using *Maxwell rheology*, is generally solved using normal-mode techniques which involves a Laplace transformation of Eq. (1) and expanding the system of equations (1) and (2) in spherical harmonics (e.g. Wu and Peltier, 1982; Vermeersen and Sabadini, 1997). We will call these therefore *spectral* (SP) methods. The system of equations is solved from the core-mantle boundary upwards using a propagator matrix technique (Sabadini and Vermeersen, 2004, p. 18). For a surface load, boundary conditions at the surface of the earth are that the normal stress is equal to the load-induced pressure and that the shear stress is zero (Wu, 2004; Sabadini and Vermeersen, 2004, p. 31). The boundary conditions for the gravity potential are treated further on in Eq. (7).

The finite-element (FE) method solves the stiffness equation, which is by the principle of virtual work equivalent to the equation of motion (Wu, 2004):

$$\vec{\nabla} \cdot \vec{\vec{\sigma}}_\delta = 0 \tag{3}$$

It thus neglects the *advection of pre-stress* (second term in Eq. (1)), the effect of internal buoyancy (third term) and the effect of *self-gravitation* (fourth term). In Section 3 we will describe how we will handle these terms when using the FE method.

To compute *geoid heights* with the flat FE model, we solve Eq. (2) by *separation of variables*. This leads for planar boundaries to a 2D Fourier transform of the gravity potential $\phi_\delta$ on the horizontal (x- and y-) coordinates:

$$\frac{\partial^2}{\partial z^2}\Phi(k_x, k_y, z) = (k_x^2 + k_y^2)\Phi(k_x, k_y, z) \tag{4}$$

with $k_x = 2\pi/\lambda_x$, $k_y = 2\pi/\lambda_y$, and $\lambda_x$, $\lambda_y$ the wavelength in the x- and y-direction, respectively. The general solution to this differential equation is

$$\Phi(k_x, k_y, z) = A(k_x, k_y)e^{k_z z} + B(k_x, k_y)e^{-k_z z} \tag{5}$$

with $k_z = \sqrt{k_x^2 + k_y^2}$.

Suppose we have a finite earth layer with the surface at $z = 0$ and the bottom at $z = z_1$, overlying an infinite substratum. In the substratum, $B_2(k_x, k_y)$ should be zero to ensure that the potential is zero for $z \to -\infty$. At the boundary with the finite layer ($z = z_1$), we have the following boundary conditions (Wu, 2004; Cathles, 1975, p. 19):

$$\Phi_1(z_1) = \Phi_2(z_1),\ \partial_z\Phi_1(z_1) - \partial_z\Phi_2(z_1) = 4\pi G(\rho_2 - \rho_1)U_1 \tag{6}$$

with $\Phi_1$, $\Phi_2$ the potential in the finite layer, respectively the substratum, $\rho_1$, $\rho_2$ the respective densities, and $U_1$ the vertical displacement at the boundary. From this we find that $B_1(k_x, k_y) = -(2\pi G/k_z)(\rho_2 - \rho_1)U_1 e^{k_z z_1}$ in the finite layer.

At the surface of the earth ($z = 0$) the transformed boundary conditions are (Wu, 2004; Cathles, 1975, p. 19):

$$\Phi_0(0) = \Phi_1(0), \partial_z\Phi_0(0) - \partial_z\Phi_1(0) = 4\pi G(\Gamma + \rho_1 U_0) \tag{7}$$

with $\Phi_0$ the potential above the surface and $\Phi_1$ below the surface, and $\Gamma$ the transformed surface density layer (i.e. water or ice).

As the solution should be finite outside the earth ($A_0(k_x, k_y) = 0$), we find from Eq. (7) that $A_1(k_x, k_y) = -(2\pi G/k_z)(\Gamma + \rho_1)U_0$ in the finite layer, so

that the total solution becomes:

$$\Phi(k_x, k_y, z) = -\frac{2\pi G}{k_z}\left((\Gamma + \rho_1 U_0)e^{k_z z} + (\rho_2 - \rho_1)U_1 e^{k_z(z_1 - z)}\right) \tag{8}$$

or, at the surface of the earth:

$$\Phi(k_x, k_y, 0) = -\frac{2\pi G}{k_z}\left(\Gamma + \rho_1 U_0 + (\rho_2 - \rho_1)U_1 e^{k_z z_1}\right) \tag{9}$$

For a multilayer model with $N$ layers, this can be generalized to:

$$\Phi(k_x, k_y, 0) = -\frac{2\pi G}{k_z}\left(\Gamma + \sum_{n=0}^{N}(\rho_{n+1} - \rho_n)U_n e^{k_z z_n}\right) \tag{10}$$

We will refer to the individual parts in the summation as *displacement potentials*.

To make the FE earth model self-gravitating, the displacement potential has to be computed at every density contrast and applied as an extra load on the corresponding boundaries, after which the FE model has to be updated, and so on (see Wu, 2004, for a spherical FE model). This is very time-consuming, and is shown below not to be necessary for a flat model of Northern Europe, because of the relatively small size of the former Fennoscandian ice sheet and the relatively small density contrasts at shallow depths (compare Table 1), and because the effect of self-gravitation is partly compensated by the lack of sphericity in the flat FE model (Amelung and Wolf, 1994). As the neglect of self-gravitation increases the rate of displacement and the lack of sphericity seems to increase the displacement (see Figure 7 of Amelung and Wolf, 1994), the two effects seem to partly compensate each other under the load only upon unloading the earth (positive rate of displacement, negative displacement) and enhance each other upon loading (negative displacement rate

and displacement).

## 3 Model Description

The 3D-flat FE model used in this study is based on the commercially available package ABAQUS. The area of loading is 5,840x5,840 km with a resolution of 80 km (73x73 elements), while the total surface area of the model is 10,000x10,000 km (97x97 elements) to minimize edge effects. The model consists of 14 finite elements in the vertical direction, of which 11 are used to model the crust and upper mantle (to 670 km depth) and 3 to simulate the lower mantle (to 10,000 km depth). This gives a total of 131,726 elements, all 8-node linear bricks. We fix the bottom of the model and restrict the movement of the edges to the vertical direction. Computations which include LVZs are very time-consuming: A model with a LVZ of $10^{19}$ Pas takes about two weeks of CPU-time on a single core 2.8 GHz processor, which gives a computation time of more than four days on a parallel machine with two dual core 2.8 GHz INTEL XEON processors. For comparison, the SP model we use takes less than half an hour on a single core processor, independent of the viscosity stratification. As we are mainly interested in perturbations due to shallow LVZs, which might make the exact modeling of the lower mantle of minor importance, we test if we can approximate the lower mantle with *infinite* elements or with *dashpots*. The latter model is based on ideas of Hetzel and Hampel (2005) and Hampel and Hetzel (2006) for earthquake triggering by GIA.

To test the accuracy of the FE model, we compare predictions with results from an analytical, spectral model, based on normal-mode analysis (see Section 2 and Wu and Peltier, 1982; Vermeersen and Sabadini, 1997). This model

provides predictions on an *incompressible* ($\rho_1 = 0$ in Eq. (1)), Maxwell viscoelastic, spherical, self-gravitating earth and is benchmarked with other GIA models (see Spada and Boschi, 2006, for comparison with an independent method). To compare the output of the SP model with the output of the flat FE model (Ivins and James, 1999), we map the former to a Cartesian grid using the Lambert equal area projection. We take the FE model also to be incompressible, and moreover, to be not self-gravitating, as explained in Section 2. We simulate the advection of pre-stress by attaching Winkler foundations to each density boundary (Ricchio and Cozzarelli, 1980; Williams and Richardson, 1991; Wu, 2004). The Winkler foundations acts like springs with a spring constant equal to the product of the gravity acceleration at and the density contrast across the boundary. Upon loading, the foundations act instantaneously, i.e. in the elastic limit of a viscoelastic material. In a purely viscous or inviscid material, the foundations only work after a certain amount of time, acting as buoyancy forces, as there can be no instantaneous displacement in a viscous material (see the footnote in Cathles, 1975, p. 14).

The radial earth stratification used is given in Table 1, where the background model consists of a 30 km fully elastic crust, a lithospheric thickness $LT =$ 80 km, and an upper [1] and lower mantle viscosity $\eta_{\mathrm{UM}} = \eta_{\mathrm{LM}} = 10^{21}$ Pas. The perturbed model can have a lower crust or asthenosphere with a low viscosity of $10^{19}$ Pas (CLVZ respectively ALVZ), either laterally homogeneous or heterogeneous. Moreover, the thickness of the lithosphere can increase to 140 km for a cratonic area, and the crustal thickness can vary from 10 km in oceanic areas to 50 km in cratonic areas. Values for the density $\rho$ and rigidity

[1] this includes the asthenosphere, the low-velocity zone, the upper mantle and the transition zone as defined in Table 1.

$\mu$ are volume-averaged from PREM (Dziewonski and Anderson, 1981).

## 4 Test Results

To test the validity of using a flat FE model for low-viscosity layers in GIA studies, the results are compared with the output of a spherical SP model for a Heaviside loading (Wolf, 1985; Ivins and James, 1999). The Heaviside load is put on the North Pole at $t = 0$ s and stays there infinitely long. In most cases, we evaluate predictions after 10 kyrs. The load consists of an elliptical ice load, with a maximum height (at the center) of 2500 m, and a radius of 8° ($\sim$ 890 km, comparable with the dimensions of the former Fennoscandian ice sheet), complemented with a eustatic ocean load of about -7.5 m. We will first consider *total* predictions from the background model, after which we will concentrate on *perturbations* due to CLVZs and ALVZs. We model a CLVZ from a depth of 20 to 30 km (10 km thickness) and a viscosity of $10^{19}$ Pas. The perturbations are the difference between the predictions of a model with a CLVZ and the background model, which has a fully elastic crust. An ALVZ is modeled at the bottom of the lithosphere (80 km) to 140 km, with a viscosity of $10^{19}$ Pas. Perturbations are now due to the difference in viscosity with the background model, which has a viscosity of $10^{21}$ Pas in this depth range, see Table 1.

In Figure **2a** we show a comparison of the vertical displacement at $t = 0$ s as predicted by the background model for the SP and FE method. Also the difference between the two methods is plotted, in *decimeters*. The deformation is determined completely by the density and rigidity of the earth model and shows a relatively large difference ($\sim$ 1 m) below the center of loading.

This difference can probably be attributed to the lack of self-gravitation in our implementation of the FE method, which leads to a larger gravitational downpull (Wu and Ni, 1996). The effect of incompressibility (Poisson's ratio $\nu = 0.5$) is large in the elastic limit. If we take the earth to be a Poisson solid (Haskell, 1953; Dahlen and Tromp, 1998, p. 4, 297), which is an approximation often used to simplify seismological problems and in which the Lamé parameter $\lambda = \mu$ with the result that $\nu = 0.25$, the vertical displacement will be about 50% larger. Note that we did only test *material* compressibility and that we did not include *internal buoyancy* (third term in Eq. (1), see for a short discussion Wu, 2004). The difference between the FE and SP model for the subsequent ($t > 0$ s) viscoelastic deformation is smaller, see Figure **2b**, where the total vertical displacement after 10 kyrs minus the elastic displacement is plotted. Besides a long-wavelength difference, there are some smaller differences in the steep part of the curve, which might be due to a lack of bending in the FE model. This suggests the use of a higher resolution grid or quadratic elements, but, because the induced errors are very small, only linear elements are used in this study. The effect of material compressibility is small for the viscoelastic deformation, decreasing the vertical displacement with only 5% under the center of the load.

If now *infinite elements* are used in the lower mantle, instead of 3 layers of elements for the lower mantle as above (from 670 km to 10,000 km, *deep* model), we see from Figure **2c** that the response is reasonably good in the elastic limit, only showing deviation in the center. The viscoelastic response however is not large enough, see Figure **2d**. In contrast, the model with *dashpots* for the lower mantle does not show enough response in the elastic limit. This because there is no response of the upper mantle-lower mantle boundary at

670 km, as a dashpot, which represents a purely viscous material, only acts after a certain amount of time (see the discussion about Winkler foundations in Section 3). The model shows however a reasonable viscoelastic response. For this work it is especially important if *perturbations* generated with these models are accurate enough, which we will consider further on.

Continuing with the deep model, we see from Figure **3a** that total geoid heights can be computed very accurately with the FE method and the use of displacement potentials as described in Section 2. Note that the differences are again given in *decimeters* and that the direct effect of the load on the geoid heights (the $\Gamma$-term in Eq. (10)) is not included. The comparison for vertical velocities (or *uplift rates*, Figure **3b**) is also excellent, and from tests (not shown) we have found that for both geoid heights and uplift rates the effect of material compressibility is negligibly small. For horizontal velocities (Figure **4a**), the quality of the FE predictions deteriorates. This is probably at least partly due to the horizontal boundary conditions in the FE model and partly due to the lack of sphericity. However, the FE model shows the behavior that is generally expected (Wu, 2005; Mitrovica et al., 1994, Figure 1) and found (Milne et al., 2001) for loading of the earth in GIA studies, i.e. an inward velocity near the center of the load and an outward velocity just outside the loading area. This corresponds with a pattern in which the peaks in the horizontal velocities correspond to the steepest parts in the uplift rates and small horizontal velocities correspond to the flat parts in the uplift rates, i.e. the pattern of horizontal velocities can for a large extent be explained by the (inward) gradient of the uplift rates, as also plotted Figure **4a**. A strong change in vertical motion thus induces a large horizontal velocity in the direction of the largest stress, which is under the load and at the forebulge, due to buoyancy forces on upper mantle

material.

For a compressible material, the FE model is in much closer agreement with the (incompressible) SP model, which seems to indicate that the lack of sphericity is partly compensated by material compressibility. However, for an earth model which has an order of magnitude increase in viscosity from the upper to the lower mantle ($\eta_{\mathrm{UM}} = 0.5 \cdot 10^{21}$ Pas, $\eta_{\mathrm{LM}} = 5.0 \cdot 10^{21}$ Pas), the effect of compressibility is smaller, see Figure **4b**. Note that now also the SP model predicts inward motion under the load, but that the differences with the FE model are still large. We have tested if also part of the differences might be due to the neglect of degree 1 in the SP model, which changes the reference frame from the center of mass of the *initial* earth to the center of mass of the *incremental* earth (Cathles, 1975, p. 101). However, including degree 1 (following the implementation of Greff-Lefftz and Legros, 1997) does only significantly affect the far field ($> 2,500$ km) predictions, preventing the outward motion to change to an inward motion from about 7,500 to 20,000 km. We will show below that differences in horizontal velocity *perturbations* are much smaller, suggesting that it is preferable to compute perturbations on a spherical background model. Finally, it might be of interest to mention that in the elastic limit (as in Figure **2a**), the model predicts inward motion only for a *compressible* material (O'Keefe and Wu, 2002). For an incompressible material, only outward motion is predicted due to the horizontal elongation of elements under the load.

Differences in vertical displacement perturbations due to a CLVZ do not show the long-wavelength behavior, because it is largely differenced out, see Figure **5a**. The short-wavelength difference is still present, though the results of the SP method look suspicious near the edge of the load, which might indicate

an inaccuracy due to Gibbs' phenomenon. The shape of the displacement perturbations can be attributed to *channel flow*, in which, opposite to *deep flow* where relaxation times are inversely proportional to the wavelength (Cathles, 1975, p. 43), relaxation times are proportional to the square of the wavelength (Cathles, 1975, p. 49), see the relaxation spectrum of the MC-mode in Schotman and Vermeersen (2005) and the results in Klemann et al. (2007). This leads to a lack of outward material flow below the center of the load and a relatively large deformation at the edge of the load (see Figure IV-21 in Cathles, 1975, p. 158) and in some cases even to a tilting of the upper crust under the center of the load (e.g. in the presence of a weaker upper mantle, compare the geoid height perturbations in Figure 7a). The comparison of Figure 5a with Figure IV-21 in Cathles (1975) needs some comment, as there *total* flow of a channel is shown, whereas we consider *perturbations* due to a channel in a background model that also consists of a lithosphere and mantle. We argue however that the comparison is valid, as a large part of the response of the lithosphere and mantle is differenced out, and because the sensitivity to the background model is not changing the *pattern* of the perturbations, see Figure **7a**.

The computed geoid height perturbations agree very well, smoothing the short-wavelength differences visible for the vertical displacement perturbations, see Figure **5c**. Amplitudes are small, but significantly larger than the expected accuracy of the GOCE mission, which is smaller than 1 cm for wavelengths longer than a few 100 km. The maximum difference with the SP model is a few centimeters, which is comparable to the accuracy of GOCE, especially if we take into account the suspicious behavior of the SP method near the edge of the ice load (see Figure **5a**). From Figure **5b** we see that for an ALVZ, the

quality of the predictions of the FE model seems to deteriorate. We found that at least 4 element-layers are needed to model the 60 km thick ALVZ and that the improvement using 6 layers is only marginal. The remaining discrepancy can probably be attributed to the lack of self-gravitation in the flat model, as the difference for the 4 element-layer shows a trend from negative under the load towards zero in the far field, as was also found for the elastic limit of the total displacements (Figure **2a**). The short wavelength difference is probably due to the use of linear elements, as explained in discussing the differences between the results of the FE and SP method in Figure **2b**. The same conclusions seem to hold for ALVZ-induced geoid height perturbations as shown in Figure **5d**.

As discussed before, it would be useful if we could replace the layering of the lower mantle with either infinite elements or dashpots in computing perturbations. In Figure **6a** we compare the perturbations in vertical displacement due to a CLVZ computed with a deep model (lower mantle to 10,000 km), a model with infinite elements for the lower mantle, and a model with dashpots for the lower mantle. Differences are small, though in general larger than the differences between the deep model and the SP model. However, for geoid height perturbations (Figure **6b**), differences are larger than a few centimeters and it seems necessary for our purposes to use the deep model. The differences can probably be explained by the contribution of the displacement potential (see Eq. (10) and the discussion there) of the upper mantle-lower mantle (670 km) boundary to the geoid height perturbations, of which the movement is not modeled very accurately for especially the model with infinite elements (see Figure **2d**). The contribution of this boundary is small compared to the surface contribution, but not much smaller in magnitude than the contribu-

tion of the much shallower (30 km) crust-lithosphere boundary. This is due to the larger density contrast at 670 km (1020 vs. 680 kg/m$^3$ at 30 km, see Table 1) and due to the longer wavelength induced at 670 km (about five times larger than at 30 km). For an ALVZ, the displacement potential of the upper mantle-lower mantle boundary has, due to the large effect of an ALVZ on the movement of this boundary (amplitude of $\sim$ 10 m to $\sim$ 2 m for a CLVZ), a significant contribution to the geoid height perturbations, being only smaller than the surface contribution. Predictions using a model with the lower mantle replaced by dashpots or infinite elements are thus worse than for a CLVZ, and are therefore not shown.

The perturbations are sensitive to the background model, see Figure **7a**, where we have plotted the CLVZ-induced perturbations for our reference background model ($LT$ = 80 km, $\eta_{\mathrm{UM}} = \eta_{\mathrm{LM}} = 1.0 \cdot 10^{21}$ Pas, '80/ 1.0/ 1.0'), and models with changes in $\eta_{\mathrm{LM}}$, $\eta_{\mathrm{UM}}$ and $LT$. The effect of a weaker upper mantle (compare '80/ 0.5/ 5.0' and '80/ 1.0/ 5.0') is largest, because of additional outward material flow in the upper mantle and larger bulges just outside of the load, i.e. the depression under the load is deeper and steeper. This increases the stress in the CLVZ just inside and outside the loading area (in the steep part of the depression and the bulge), enhancing mass flow through the CLVZ from the edges outwards, and tilting of the upper crust in the center. The background model does not change the pattern of channel flow, which is not the case for ALVZ-induced perturbations, see Figure **7b**. Where the perturbations for our reference background model are determined by channel flow (small perturbations under the center of the load), the perturbations for a weaker upper mantle ($\eta_{\mathrm{UM}} = 0.5 \cdot 10^{21}$ Pas) show deep flow behavior. This effect is, somewhat less pronounced, also present for only a stiffer lower mantle

($\eta_{\mathrm{LM}} = 5.0 \cdot 10^{21}$ Pas).

Perturbations in horizontal velocities show (see Figure **8**), in contrast with *total* horizontal velocities (Figure **4a**), the same behavior for the FE and SP method. Both for a CLVZ and an ALVZ, the quality deteriorates towards the far field, at least partly due to the boundary conditions in the FE model, which are fixed in the horizontal direction at 10,000 km. If we compare this with the SP model, in which, due to symmetry considerations, the horizontal direction is fixed at the south pole ($\sim 20,000$ km), we argue that part of the difference can be explained by the larger horizontal elongation or stretching of the crust/lithosphere for a shorter distance to a fixed point, i.e. for the FE model. However, due to the large differences between the FE and SP model for total horizontal velocities (Figure **4a**), other causes such as the lack of sphericity cannot be ruled out. The patterns can again for a large part be explained by the inward gradient of the uplift rates (not shown). The noisy character of the perturbations, especially for a CLVZ, are due to the double differencing and the relatively low precision ('single', default) used for the output of ABAQUS, which can be changed to 'double' in the execution procedure. Note that the differences with the SP model are small compared to the accuracy of the BIFROST network ($\sim 0.3$ mm/yr), however, so are the perturbations. This means that LVZs can probably not be detected by BIFROST, especially because high-resolution spatial information is not provided.

In Figure **9a** perturbations are shown due to a laterally heterogeneous CLVZ, that extends from just under the load ('A', 670 km) outward. This means that the laterally heterogeneous model is equal to the background model from the center of the load to 'A', and equal to the model with a laterally homogeneous CLVZ from 'A' outwards. Because under the load the induced stresses

are largest, the response is comparable to the homogeneous case from 670 km outwards. Inwards, there seems to be some tilting of the crust relative to the displacement of the crust in the background model, due to the indentation of the crust from 'A' outwards. For a CLVZ from 1110 km ('B') outwards, the effect of the lateral heterogeneity is much more pronounced, and leads to a significant relative tilting of the crust. For an ALVZ the effect of lateral heterogeneities is larger, substantially weakening the amplitudes of the homogeneous case, but mainly showing the same effect as for a CLVZ and therefore not shown. As shallow viscosity and lithospheric thickness $LT$ are via thermal regime closely related, we show in Figure **9b** the effect of the inclusion of a larger $LT$ ('craton') under the load only, and the inclusion of both a larger $LT$ under the load and a laterally heterogeneous CLVZ. The effect of a craton under the load is to strengthen the lithosphere, thus de-amplifying the vertical displacement in the center, and thus inducing a positive geoid height perturbation. If the craton extends to outside the load ('craton $<$ B (1110 km)'), there is also a negative perturbation outside the load, because, due to the larger lithospheric strength, the bulge area is broader and smoother. If we now compare the perturbations due to variations in $LT$ only with perturbations due to both a laterally heterogeneous $LT$ and CLVZ, we see that only for the case that part of the ice load is in an area of small $LT$ and a CLVZ ('craton $<$ A, CLVZ $>$ A'), differences are as large as 10 cm. Due to the different scales of deformation for variations in lithospheric thickness (wavelengths mainly larger than 1000 km) and for a CLVZ (mainly smaller than 1000 km), the two effects might be separated using medium- to high-resolution gravity field information as provided by GOCE.

## 5 Example for Northern Europe

We will now investigate the effect of lateral heterogeneities in LVZs and $LT$ using a simple regional model for Northern Europe, in which we assume 3 different types of areas, see also Figure **10a-c**:

I. Continental areas with a 50 km thick elastic crust in a thick elastic lithosphere ($LT$ = 140 km), on top of an upper mantle with a viscosity of $10^{21}$ Pas, which represent old, cratonic areas that are mainly Archean and Early Proterozoic (> 1.5 Gyr, Pérez-Gussinyé and Watts, 2005). This type corresponds well with estimates of thermal thickness larger than 140 km (Artemieva and Mooney, 2001);
II. Continental areas with 20 km elastic upper crust and a 10 km lower crust that is either elastic or has low viscosity ($10^{19}$ Pas, CLVZ). The total lithospheric thickness is thinner now ($LT$ = 80 km) and overlies a 60 km thick asthenosphere that has either the viscosity of the upper mantle ($10^{21}$ Pas) or a low viscosity ($10^{19}$ Pas, ALVZ). These areas are younger (< 1.5 Gyr) and have a thermal thickness smaller than 140 km;
III. Oceanic areas with a 10 km crust in a lithosphere of 80 km, overlying a 60 km thick asthenosphere with a viscosity of $10^{21}$ Pas or $10^{19}$ Pas (ALVZ).

The different areas are derived from CRUST2.0 (http://mahi.ucsd.edu/Gabi/rem.dir/crust/crust2.html, accessed 3 May 2007), in which an area with a crustal thickness between 15 and 35 km is considered as Type II. Areas with a crustal thickness thinner than 15 km are then Type III and thicker than 35 km Type I. The different areas are indicated in Figures **10d**. Note that this is a first approximation, which means that some areas in Type II are

oceanic and that some areas in Type I are not cratonic. We use the ice-load history as derived by Lambeck (RSES, Lambeck et al., 1998), which is given from 30 kyrs BP to present for Fennoscandia, the Barents Sea area and the British Isles. We complement this with the eustatic ocean-load history of the global RSES model, which is about -130 m from 30 kyrs BP to the last glacial maximum (LGM, 21 kyrs BP), and include a linear glaciation phase of 90 kyrs to have a glacial cycle of 120 kyrs. We have plotted the ice heights at LGM in Figure **10e**.

In Figure **11a** we show total (i.e. background-induced) 3D-velocity predictions for Northern Europe computed with the FE model. Contour lines show the difference in uplift rates with the SP model, the black arrows are horizontal velocities computed with the FE model and the white arrows are computed with the SP model. As expected from Figure **3b**, the uplift rates compare well, with only some small areas where the difference is larger than 0.2 mm/yr (which is much smaller than the accuracy of about 1 mm/yr as reported for the BIFROST network, Johansson et al., 2002). Note that the predicted uplift rate is sensitive to the earth stratification, which explains differences with e.g. Milne et al. (2001), who use the same ice-load history. The horizontal rates compare less well, though not as bad as expected from Figure **4a**. In Figure **11b** we show the total geoid height predictions. Contour lines are again differences with the SP model, which are generally smaller than 2 cm, which is comparable to the accuracy of the GOCE mission. Note that we have subtracted the mean from both fields, as we have in our FE computations no self-gravitating sea level that can serve as a reference for the geoid height.

Also for LVZ-induced perturbations in 3D-velocities we see some differences between FE and SP (Figure **12**), though the general pattern agrees well.

Note that perturbations in horizontal velocities are up to 0.5 mm/yr, which is slightly larger than the accuracy of the BIFROST network of about 0.3 mm/yr. However, due to the point-like character of GPS measurements, which makes the extraction of relatively high-resolution spatial signatures difficult, and the fact that part of the perturbative signal is generated by assuming LVZs below Scandinavia, we expect that BIFROST cannot add information on LVZs. This is confirmed by Milne et al. (2001), who indicate that the radial resolving power of their inversion is $\sim$ 200 km in the shallow earth.

In Figure **13a** we show geoid height perturbations due to a laterally homogeneous CLVZ, in which contour lines indicate again differences with the SP model. The pattern can be explained by lower crustal material flow through the low-viscosity channel from under the ice load outwards during glaciation, and the long relaxation times of crustal channel flow (Schotman and Vermeersen, 2005). Due to the long glaciation period ($\sim$ 100 kyrs), the earth is close to isostatic equilibrium at LGM and during the much shorter deglaciation period ($\sim$ 20 kyrs) only part of the crustal material has returned from the perturbative bulges. For a homogenous ALVZ the differences are also small, see Figure **13b**. The pattern is broader, and moreover of opposite sign. This is due to the fact that an ALVZ accelerates the deformation process, as described in Schotman and Vermeersen (2005). To highlight the effect of lateral heterogeneities in the LVZ, we show in Figure **13c, d** the difference between a model which includes a laterally heterogeneous LVZ and a model which includes a laterally homogeneous LVZ (as shown in **a, b**). To focus on the LVZ only, we have not yet included variations in the lithospheric thickness. For a CLVZ the differences are relatively small, though still with amplitudes up to 20 cm. Of course, the differences are large in the Baltic Shield, but also in

527 southern Scandinavia, at the edge of the cratonic area, and off the Norwegian
528 coast, where the geoid high predicted by the model with a homogeneous CLVZ
529 is for the model with a laterally heterogeneous CLVZ significantly smaller. For
530 an ALVZ, the effect of lateral heterogeneities is somewhat larger, showing a
531 clear difference under the main domes of the RSES ice-load history, but also
532 further outwards, especially to the east, due to the larger depth of the ALVZ
533 compared to the CLVZ.

534 Before we look at the simultaneous effect of lateral variations in $LT$ and LVZs,
535 we show the effect of variations in $LT$ in the absence of an LVZ. The geoid
536 height perturbations in Figure **14a** are thus only due to the thicker lithosphere
537 ($LT = 140$ km) of the Baltic Shield. The effect is largest over the Baltic Sea,
538 as there the ice load is largest, see Figure **10e**. In the perturbations due to
539 lateral heterogeneities in both $LT$ and a CLVZ (Figure **14b**), we can still see
540 the effect of the CLVZ around the formerly glaciated area (geoid highs of 20-
541 30 cm, see Figure **13a**) and the effect of the large $LT$ below the largest ice
542 load (geoid high of 50 cm, compare with Figure **14a**). Due to the different
543 spatial signatures of both effects, it seems to be possible to separate the two
544 and extract information on both $LT$ and crustal low-viscosity. For an ALVZ
545 (Figure **14c**) the separation of the two effects seems to be difficult, as the effect
546 of variations in $LT$ (Figure **14a**) is very similar to ALVZ-induced perturbations
547 (Figure **13b**), especially along the Norwegian coast and under the major ice
548 domes.

## 6 Realistic Ocean-Load History

For loading the FE model for Northern Europe in Section 5, we used the eustatic ocean-load output of the SP model. Here we show which error this introduces in geoid height predictions compared with predictions of a self-gravitating model that includes realistic oceans ('RO', which includes the effect of self-gravitation in the oceans, but also the effect of time-dependent coastlines and meltwater influx, see Section 1). For total geoid heights predicted with the RSES ice-load history, the errors introduced by using the eustatic load output of the SP model is shown in Figure **15a**. The maximum error is about 20 cm, which is small compared to the total amplitudes of several meters (Figure **11b**). Moreover, the relatively large error over the Northern Atlantic (geoid height predictions in this area are about zero) can be removed if we use the realistic ocean-load output of the SP model. However, the errors in areas that were once glaciated and are now ocean covered increase to 30 cm (Barents Sea, North Sea) and 50 cm (Gulf of Bothnia). For CLVZ-induced perturbations, the error is generally smaller than 5 cm (Figure **15b**), compared to CLVZ-induced geoid height perturbations of tens of centimeters (Figure **13a**). Note the clear effect of time-dependent coastlines and meltwater influx in the the Gulf of Bothnia, which is also present if we use the realistic ocean-load output of the SP model. Overall errors are somewhat smaller then, but probably not negligibly small. For an ALVZ, the errors are up to 10 cm (Figure **15c**), but ALVZ-induced geoid height perturbations have amplitudes that are about 5 times as large, compare Figure **13b**, so these errors can probably be neglected.

## 7 Conclusion

We have shown that a 3D-flat, non-self-gravitating finite-element (FE) model of glacial-isostatic adjustment (GIA) can deliver accurate predictions of radial displacements, uplift rates and geoid heights when compared to conventional spherical, self-gravitating spectral (SP) models. Perturbations in these predictions due to shallow low-viscosity zones (LVZs) can also be computed accurately, though the accuracy seems, due to the neglect of self-graviation, to decrease somewhat with increasing depth, and moreover, the sensitivity to the background model increases considerably. Predictions of horizontal velocities are less accurate, showing considerable differences with the predictions of an SP model, probably due to the lack of sphericity of the model. We have to keep in mind however that horizontal velocities are very sensitive to model parameters in general. We have shown that material compressibility can have a significant effect on horizontal velocities. The effect on uplift rates and geoid heights is found to be negligibly small.

For a simple model of Northern Europe, horizontal and vertical velocity perturbations due to shallow LVZs are only slightly above the current BIFROST performance and due to the relatively low spatial resolution of BIFROST, we do not expect BIFROST to add information on LVZs. We have found that lateral heterogeneities do not necessarily have a large influence on CLVZ-induced perturbations, though amplitudes are still up to 20 cm in geoid height, which is an order of magnitude larger than the expected GOCE performance. In reality, however, we also have to consider unmodeled thermally- and chemically-induced shallow mass inhomogeneities, that are expected to be effective in masking the gravity signal due to CLVZs. We find, for example, from the

GRACE satellite gravity mission (solution GGM02S, Tapley et al., 2005), only retaining the spherical harmonic coefficients from degree 40 to 90, where CLVZs have their largest signal, geoid heights of a few meters. Effective spatio-spectral filtering tools have to be developed to extract the GIA-related signal (see Schotman and Vermeersen, 2005, for a discussion), in which we expect the specific signatures of CLVZs to be useful. For example, because of the different signature of perturbations due to a CLVZ and due to variations in lithospheric thickness, it seems possible to solve for both lithospheric thickness and CLVZs at the same time.

Forcing the FE model with a eustatic ocean load gives in general acceptable results, which can be improved somewhat using the realistic load output of the self-gravitating SP model. Errors in CLVZ-induced geoid height perturbations are about 5 cm, which is small but not negligible compared to the amplitudes of the perturbations (tens of centimers). For an ALVZ, the errors are somewhat larger, but small compared to the perturbations. Based on the above we have given in Table 2 overview of error estimates using the flat, not self-gravitating FE model and the spherical, self-gravitating SP model ('FE vs. SP'), for geoid heights and geoid height perturbations ('GEO') and horizontal velocities and velocity perturbations ('VEL'). We have also given the error estimates of using a eustatic instead of realistic ocean load ('EU vs. RO'). If we accept errors equal to or smaller than 10%, we have to be critical when computing (perturbations in) horizontal velocities and when using a eustatic ocean load for computing CLVZ-induced geoid height perturbations. For this error bound, we cannot use infinite or dashpot elements to replace the deep layering of the lower mantle (to 10,000 km), as the errors are larger than 10% for LVZ-induced perturbations.

## Acknowledgments

We thank Taras Gerya, Erik Ivins and an anonymous reviewer for their useful comments, Kurt Lambeck and co-workers (RSES, Australian National University, Canberra) for providing the RSES ice-load history, Marianne Greff-Lefftz (IPGP, Paris) for benchmarking degree-1 deformation, Pieter Visser (DEOS, Delft University of Technology) for providing estimates of the GOCE performance, and Radboud Koop (NIVR, Delft, previously at SRON, Utrecht), Rob Govers (IVAU, Utrecht University) and the Geoscientific Abaqus User Group (Geoqus), especially Andrea Hampel (Institut für Geologie, Mineralogie und Geophysik, Ruhr-Universität Bochum), for discussions.

## References

Amelung, F., and Wolf, D., 1994. Viscoelastic perturbations of the earth: significance of the incremental gravitational force in models of glacial isostasy. Geophys. J. Int., 117: 864–879.

Artemieva, I.M., and Mooney, W.D., 2001. Thermal structure and evolution of Precambrian lithosphere. J. Geophys. Res., 106: 16387–16414.

Cathles, L.M., 1975. The Viscosity of the Earth's Mantle. Princeton University Press, Princeton, 390 pp.

Dahlen, F.A., and Tromp, J., 1998. Theoretical Global Seismology. Princeton University Press, 1025 pp.

Dziewonski, A.M., and Anderson, D.L., 1981. Preliminary Reference Earth Model. Phys. Earth Planet. Inter., 25: 297–356.

Greff-Lefftz, M., and Legros, H., 1997. Some remarks about the degree-one deformation of the Earth. Geophys. J. Int., 131: 699–723.

Hampel, A., and Hetzel, R., 2006. Response of normal faults to glacial-interglacial fluctuations of ice and water masses on Earth's surface. J. Geophys. Res., 111: 10.1029/2005JB004124.

Haskell, N.A., 1953. The dispersion of surface waves on Multilayered Media. Bull. Seism. Soc. Am., 43: 17–34.

Hetzel, R., and Hampel, A., 2005. Slip rate variations on normal faults during glacial-interglacial changes in surface loads. Nature, 435: 81–84.

Ivins, E.R., and James, T.S., 1999. Simple models for late Holocene and present-day Patagonian glacier fluctuations and predictions of a geodetically detectable isostatic response. Geophys. J. Int., 138: 601–624.

Johansson, J.M., Davis, J.L., Scherneck, H.-G., Milne, G. A., Vermeer, M., Mitrovica, J.X., Bennett, R.A., Jonsson, B., Elgered, G., Elósegui, P., Koivula, H., Poutanen, M., Rönnäng, B.O., and Shapiro, I.I., 2002. Continuous GPS measurements of postglacial adjustment in Fennoscandia 1. Geodetic results. J. Geophys. Res., 107: 10.1029/2001JB000400.

Klemann, V., Ivins, E.R., Martinec, Z., and Wolf, D., 2007. Models of active glacial isostasy roofing warm subduction: Case of the South Patagonian Ice Field. J. Geophys. Res., 112: 10.1029/2006JB004818.

Lambeck, K., Smither, C., and Johnston, P., 1998. Sea-level change, glacial rebound and mantle viscosity of northern Europe. Geophys. J. Int., 134: 102–144.

Latychev, K., Mitrovica, J.X., Tromp, J., Tamisiea, M., Komatitsch, D., and Christara, C.C., 2005. Glacial isostatic adjustment on 3-D Earth models: A finite-volume formulation. Geophys. J. Int., 161: 421–444.

Meissner, R., and Kusznir, N.J., 1987. Crustal viscosity and the reflectivity of the lower crust. Ann. Geophys., 5B: 365–374.

Milne, G.M., Davis, J.L., Mitrovica, J.X., Scherneck, H.-G., Johansson, J.M.,

675 Vermeer, M., and Koivula, H., 2001. Space-geodetic constraints on glacial
676 isostatic adjustment in Fennoscandia. Science, 291: 2381–2385.
677 Mitrovica, J.X., and Milne, G.A., 2003. On post-glacial sea level: I. General
678 theory. Geophys. J. Int., 154: 253–267.
679 Mitrovica, J.X., Davis, J.L., and Shapiro, I.I., 1994. A spectral formalism for
680 computing three-dimensional deformations due to surface loads 2. Present-
681 day glacial isostatic adjustment. J. Geophys. Res. 99: 7075–7101.
682 Mitrovica, J.X., Wahr, J., Matsuyama, I., and Paulson, A., 2005. The rota-
683 tional stability of an Ice-Age Earth. Geophy. J. Int., 161: 491–506.
684 O'Keefe, K., and Wu, P., 2002. Effect of mantle structure on postglacial in-
685 duced horizontal displacement. In: J.X. Mitrovica and L.L.A. Vermeersen
686 (Editors). Ice Sheets, Sea Level and the Dynamic Earth. AGU Geodynamics
687 Series, 29: 109–118.
688 Pérez-Gussinyé, M., and Watts, A.B., 2005. The long-term strength of Europe
689 and its implications for plate-forming processes. Nature, 436: 381–384.
690 Ranalli, G., and Murphy, D., 1987. Rheological stratification of the lithosphere.
691 Tectonophys., 132: 281–295.
692 Ricchio M., and Cozzarelli, F.A., 1980. A model of creep deformation in the
693 lithosphere as a non-isothermal linear viscous circular plate on a Winkler
694 foundation. Phys. Earth Planet. Inter., 23: 87–97.
695 Sabadini, R., and Vermeersen, L.L.A., 2004. Global Dynamics of the Earth:
696 Applications of Normal Mode Relaxation Theory to Solid-Earth Geophysics.
697 Kluwer Academic, Modern Approaches in Geophysics Series, 20, 328 pp.
698 Schotman, H.H.A., and Vermeersen, L.L.A., 2005. Sensitivity of glacial iso-
699 static adjustment models with shallow low-viscosity earth layers to the ice-
700 load history in relation to the performance of GOCE and GRACE. Earth
701 Planet. Sci. Lett., 236: 10.1016/j.epsl.2005.04.008.

Spada, G., and Boschi, L., 2006. Using the Post-Widder formula to compute the Earth's viscoelastic Love numbers. Geophys. J. Int., 166: 309–321.

Steffen, H., and Kaufmann, G., 2005. Glacial isostatic adjustment of Scandinavia and northwestern Europe and the radial viscosity structure of the Earth's mantle. Geophys. J. Int., 163: 801–812.

Tamisiea, M.E., Mitrovica, J.X., and Davis, J.L., 2007. GRACE Gravity Data Constrain Ancient Ice Geometries and Continental Dynamics over Laurentia. Science, 316: 881–883.

Tapley, B., Ries, J., Bettadpur, S., Chambers, D., Cheng, M., Condi, F., Gunter, B., Kang, Z., Nagel, P., Pastor, R., Pekker, T., Poole, S., and Wang, F., 2005. GGM02 - An improved Earth gravity field model from GRACE. J. Geodesy, 10.1007/s00190-005-0480-z.

Vermeersen, L.L.A., and Sabadini, R., 1997. A new class of stratified viscoelastic models by analytical techniques. Geophys. J. Int., 139: 530–571.

Visser, P.N.A.M., Rummel, R, Balmino, G., Sünkel, H., Johannessen, J., Aguirre, M., Woodworth, P.L., Le Provost, C., Tscherning, C.C., and Sabadini, R., 2002. The European Earth explorer mission GOCE: Impact for the geosciences. In: J.X. Mitrovica and L.L.A. Vermeersen (Editors). Ice Sheets, Sea Level and the Dynamic Earth. AGU Geodynamics Series, 29: 95–107.

Watts, A.B., and Burov, E.B., 2003. Lithospheric strength and its relationship to the elastic and seismogenic layer thickness. Earth Planet. Sci. Lett., 213: 113–131.

Williams, C.A., and Richardson, R.M., 1991. A rheologically layered three-dimensional model of the San Andreas fault in Southern California. J. Geophys. Res., 96: 16597–16623.

Wolf, D., 1985. The normal modes of a layered, incompressible Maxwell half-space, J. Geophys. Res., 57: 106–117.

729 Wolf, D., 1998. Gravitational-viscoelastic field theory. In: P. Wu. (Editor).
730 Dynamics of the Ice Age Earth: A Modern Perspective. Trans Tech Publi-
731 cations, GeoResearch Forum, 3-4: 55–86.
732 Wu, P., 2002. Mode coupling in a viscoelastic self-gravitating spherical earth
733 induced by axisymmetric loads and lateral viscosity variations. Earth
734 Planet. Sci. Lett., 202: 49–60.
735 Wu, P., 2004. Using commercial finite element packages for the study of earth
736 deformations, sea levels and the state of stress. J. Geophys. Res., 158: 401–
737 408.
738 Wu, P., 2005. Effects of lateral variations in lithospheric thickness and mantle
739 viscosity on glacially induced surface motion in Laurentia. Earth Planet.
740 Sci. Lett., 235: 549–563.
741 Wu, P., and Ni, Z., 1996. Some analytical solutions for the viscoelastic gravita-
742 tional relaxation of a two-layer non-self-gravitating incompressible spherical
743 earth. Geophys. J. Int., 126: 413–436.
744 Wu, P., and Peltier, W.R., 1982. Viscous gravitational relaxation. Geophys.
745 J. R. Astron. Soc., 70: 435–485.
746 Wu, P., and van der Wal, W., 2003. Postglacial sealevels on a spherical, self-
747 gravitating viscoelastic Earth: Effects of lateral viscosity variations in the
748 upper mantle on the inference of viscosity contrasts in the lower mantle.
749 Earth Planet. Sci. Lett., 211: 57–68.
750 Wu, P., Wang, H., and Schotman, H., 2005. Postglacial induced surface mo-
751 tions, sea-levels and geoid rates on a spherical, self-gravitating, laterally
752 heterogeneous Earth. J. Geodyn., 39: 127–142.
753 Zhong, S.J., Paulson, A., and Wahr, J., 2003. Three-dimensional finite element
754 modeling of Earth's viscoelastic deformation: Effects of lateral variations in
755 lithospheric thickness, Geophys. J. Int., 155: 679–695.

**(a)** near-field **(b)** far-field

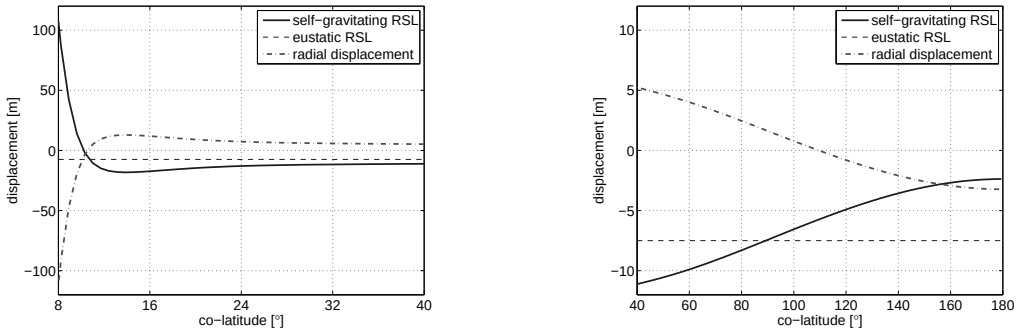


Fig. 1. Near- **(a)** and far- **(b)** field effect of an elliptical iceload (8° radius) on the North Pole after 10 kyrs of loading

**(a)** *E*, FE vs. SP **(b)** *VE*, FE vs. SP

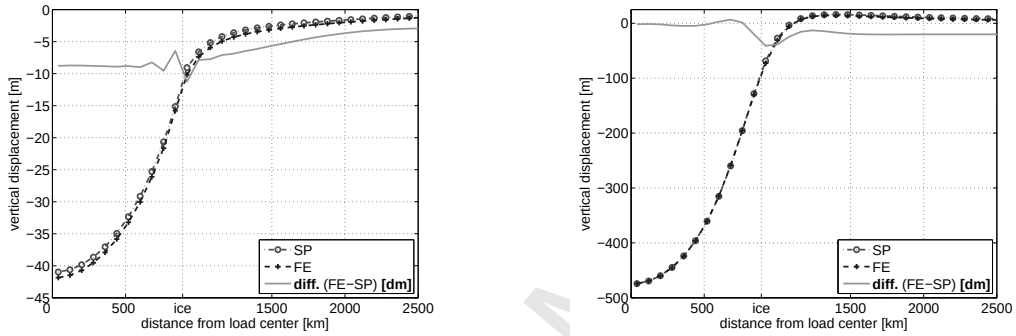


**(c)** *E*, deep vs. shallow **(d)** *VE*, deep vs. shallow

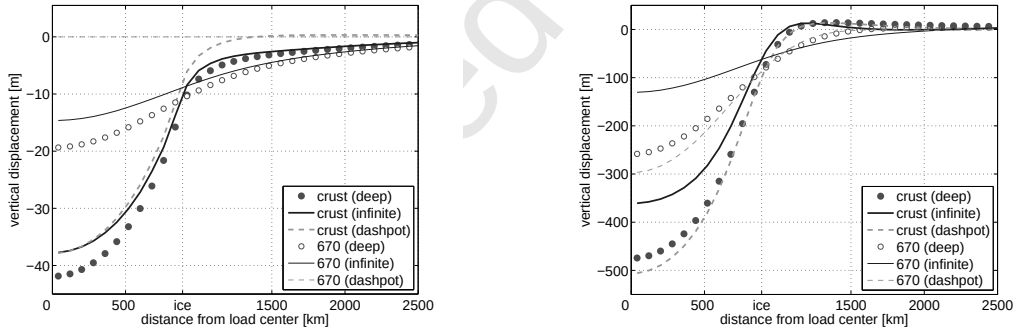


Fig. 2. Elastic ($t = 0$ s, '*E*', left) and viscoelastic ($t > 0$ s, total response minus response at $t = 0$ s, '*VE*', right) response for the SP and FE model **(a, b)** and a *deep* model (lower mantle to 10,000 km), and *shallow* models using *infinite* elements for the lower mantle, or using *dashpots* for the lower mantle **(c, d)**

**(a)** geoid heights **(b)** uplift rates

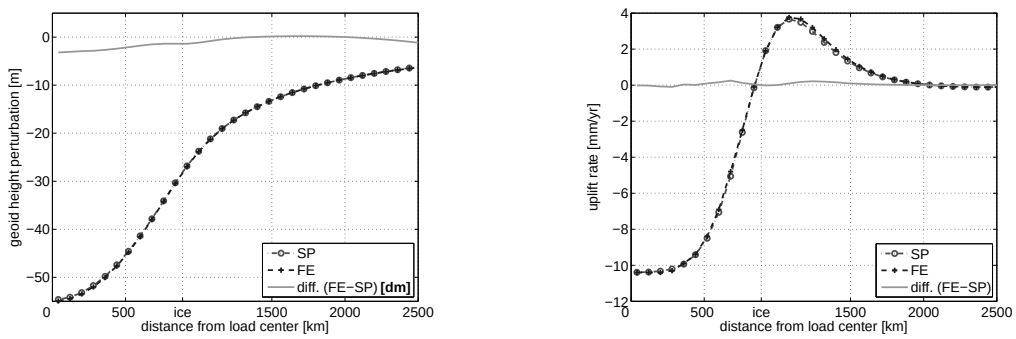


Fig. 3. Comparison of geoid heights **(a)** and uplift rates **(b)** as predicted by the SP and FE method

**(a)** univiscous **(b)** order of magnitude

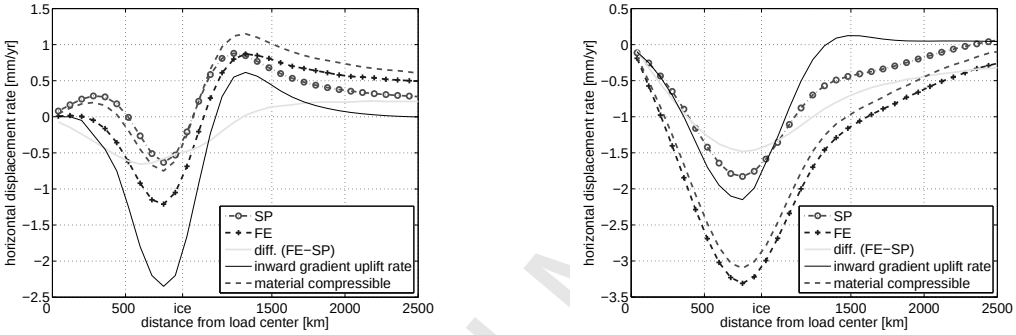


Fig. 4. Horizontal velocities (positive is outward motion) as predicted by the SP and FE method for a univiscous (Table 1) earth model **(a)** and an earth model with an order of magnitude increase in viscosity from the upper to lower mantle **(b)**

**(a)** CLVZ, vertical displacement perturbations

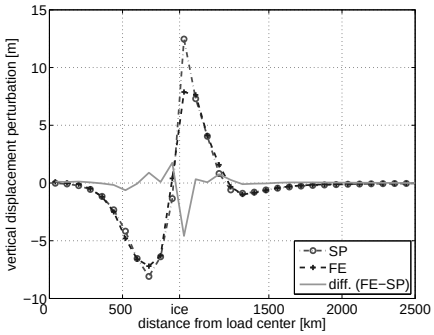


**(b)** ALVZ, vertical displacement perturbations

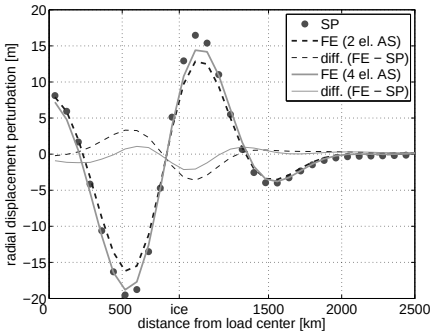


**(c)** CLVZ, geoid height perturbations

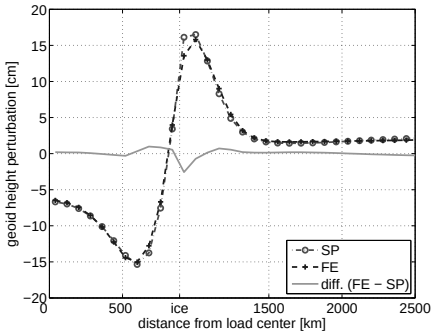


**(d)** ALVZ, geoid height perturbations

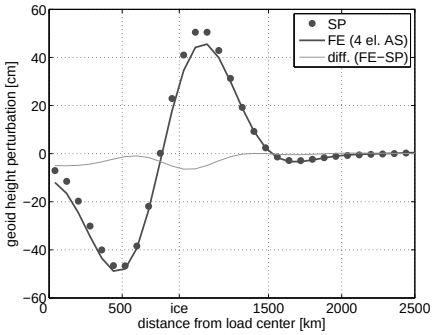


Fig. 5. CLVZ- (left) and ALVZ- (right) induced vertical displacement **(a, b)** and geoid height **(c, d)** perturbations due to a laterally homogeneous LVZ

**(a)** vertical displ. perturbations **(b)** geoid height perturbations

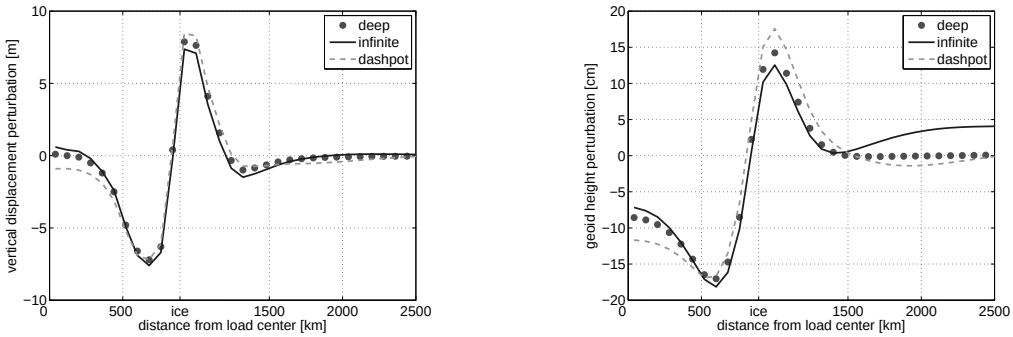


Fig. 6. CLVZ-induced vertical displacement **(a)** and geoid height **(b)** perturbations for a *deep* model (lower mantle to 10,000 km), a model using *infinite* elements for the lower mantle, and a model using *dashpots* for the lower mantle

**(a)** CLVZ **(b)** ALVZ

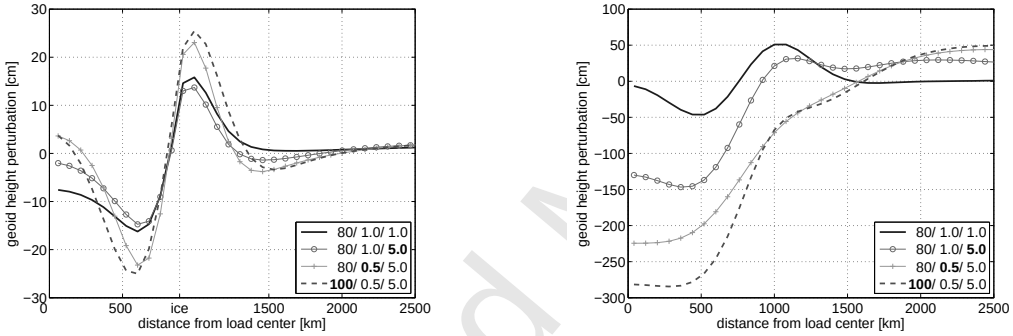


Fig. 7. Effect of the background earth model on CLVZ- **(a)** and ALVZ- **(b)** induced perturbations (the legend gives: LT [km]/ $\eta_{\mathrm{UM}}$ [$10^{21}$ Pas]/ $\eta_{\mathrm{LM}}$ [$10^{21}$ Pas])

**(a)** CLVZ **(b)** ALVZ

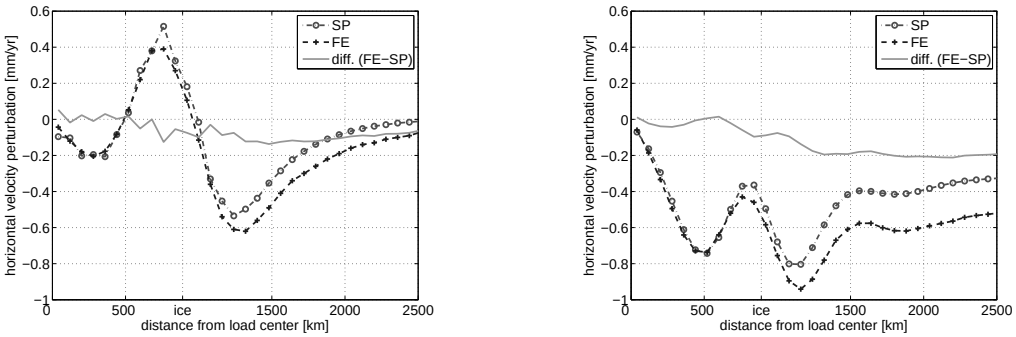


Fig. 8. CLVZ- **(a)** and ALVZ- **(b)** induced horizontal velocity perturbations (positive direction is outward motion)

**(a)** CLVZ **(b)** *LT* and CLVZ

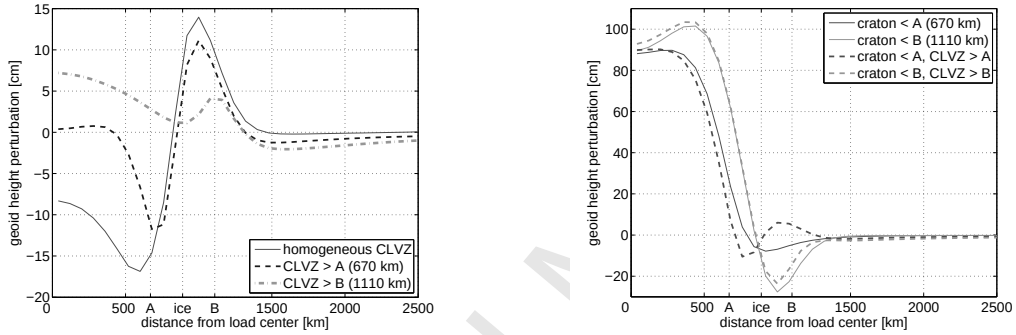


Fig. 9. Geoid height perturbations due to a laterally heterogeneous CLVZ **(a)** and due to a laterally heterogeneous *LT* and CLVZ **(b)**

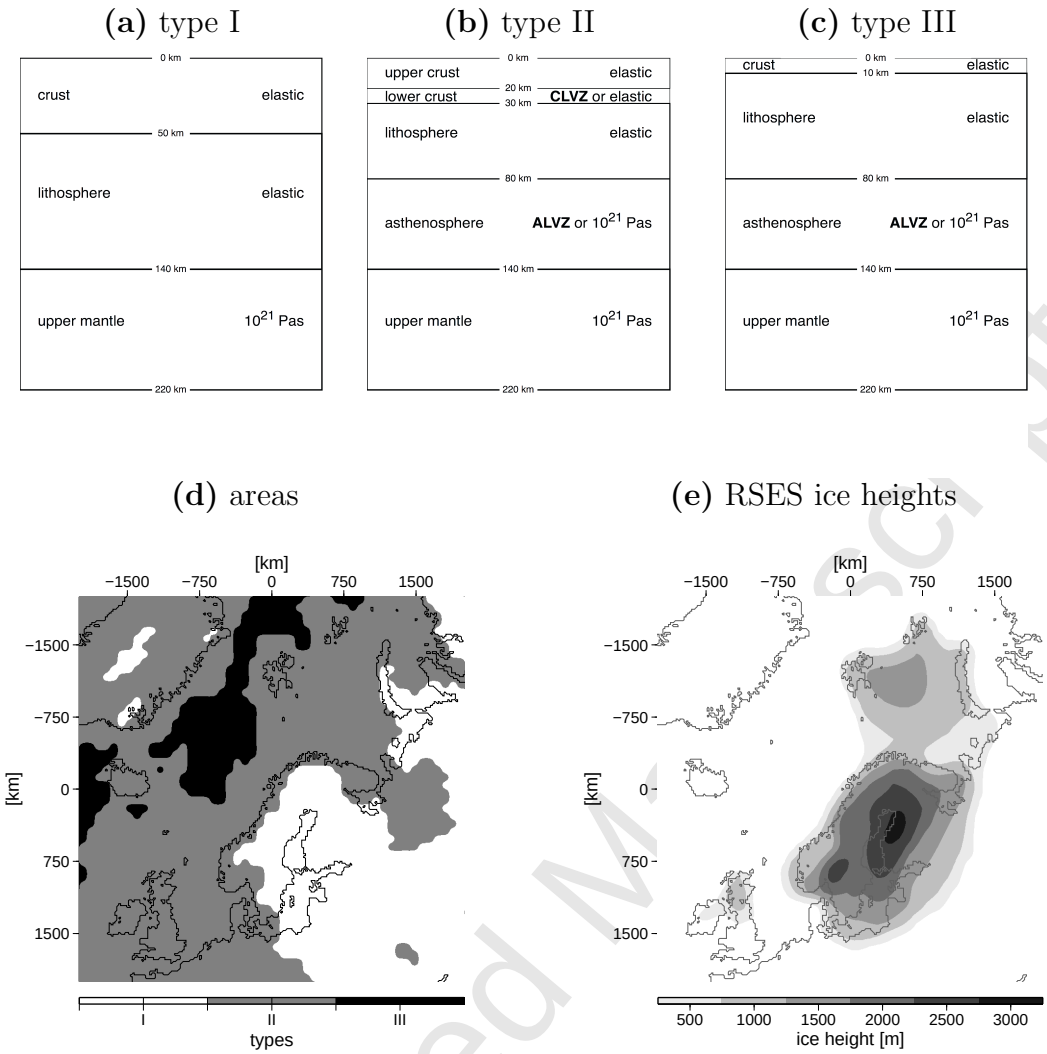


Fig. 10. Earth stratification for the 3 areas: type I **(a)**, type II **(b)** and type III **(c)**, corresponding geographical areas based on CRUST2.0 **(d)**, and RSES ice heights at LGM **(e)**

**(a)** 3D-velocities **(b)** geoid heights

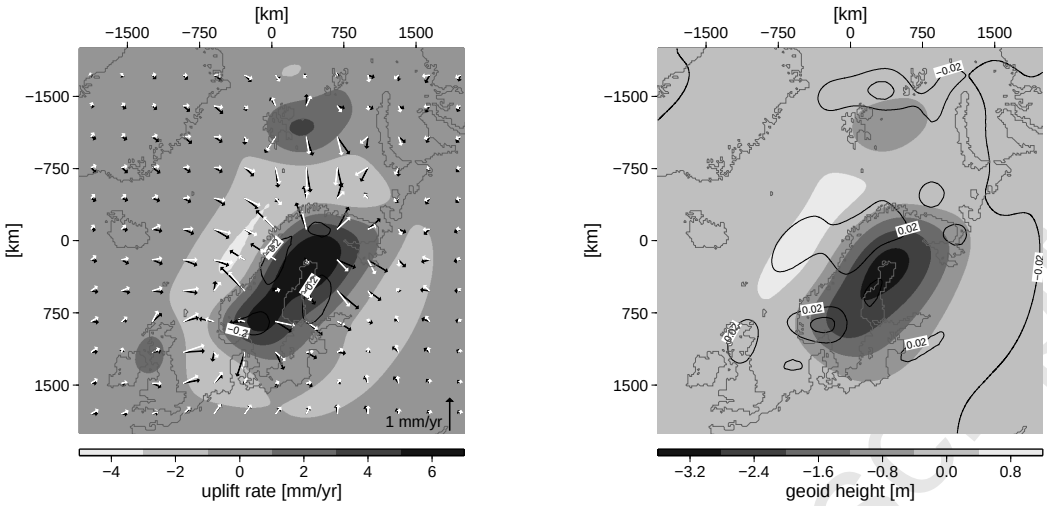


Fig. 11. Total (no LVZ) 3D-velocities **(a)** and geoid heights **(b)** at present, computed with FE (white arrows are computed with SP, contour lines are difference with SP)

**(a)** CLVZ **(b)** ALVZ

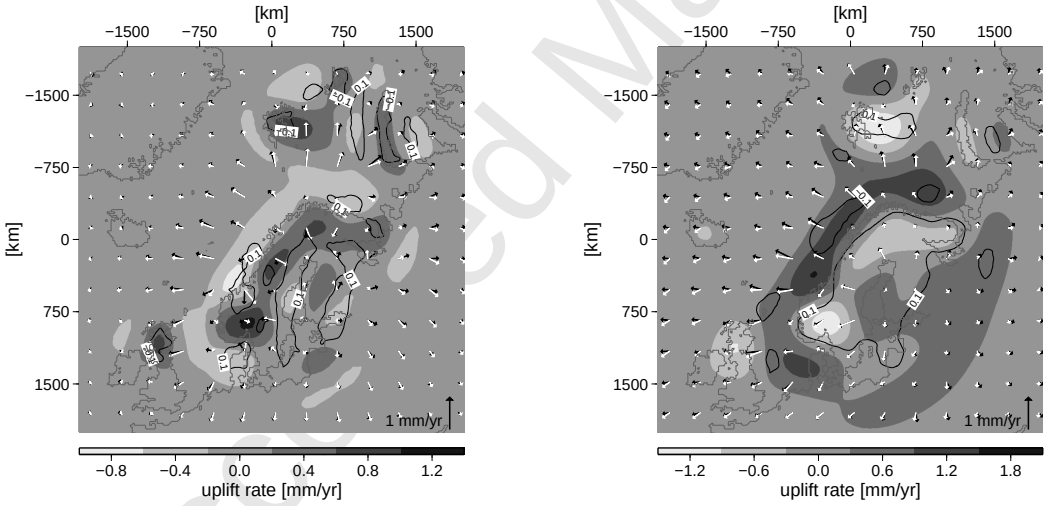


Fig. 12. CLVZ- **(a)** and ALVZ- **(b)** induced 3D-velocity perturbations (white arrows are computed with SP, contour lines are difference with SP)

**(a)** CLVZ, lat. hom. **(b)** ALVZ, lat. hom.

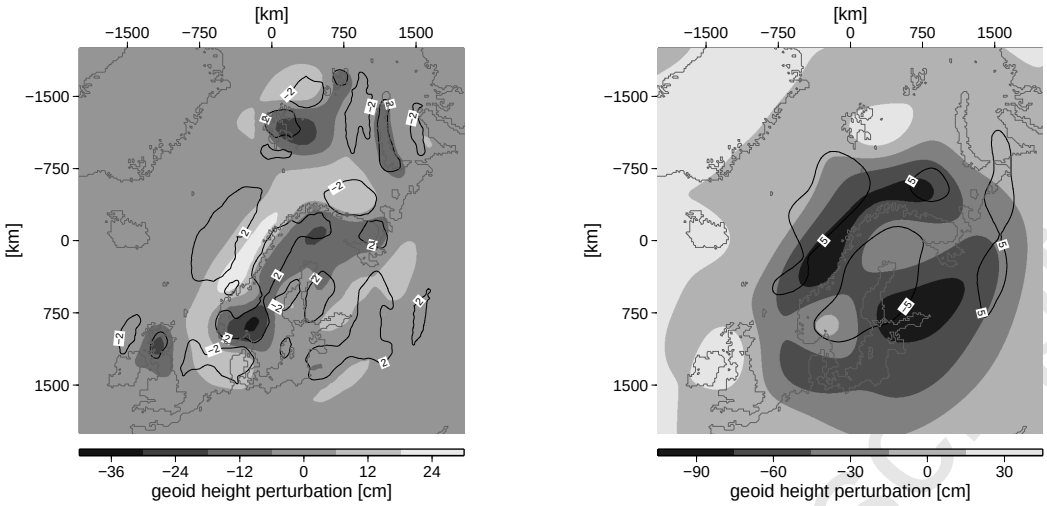


**(c)** CLVZ, effect of lat. het. **(d)** ALVZ, effect of lat. het.

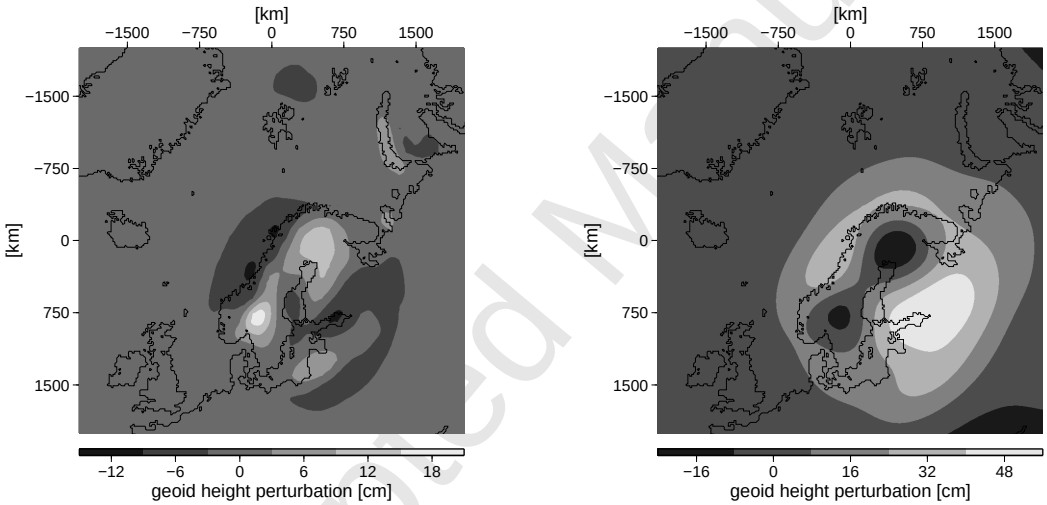


Fig. 13. Geoid height perturbations for a laterally homogeneous CLVZ **(a)** and ALVZ **(b)**, and differences between a laterally heterogeneous and homogeneous CLVZ **(c)** and ALVZ **(d)**

**(a)** laterally heterogeneous $LT$

**(b)** lat. het. $LT$ and CLVZ

**(c)** lat. het. $LT$ and ALVZ

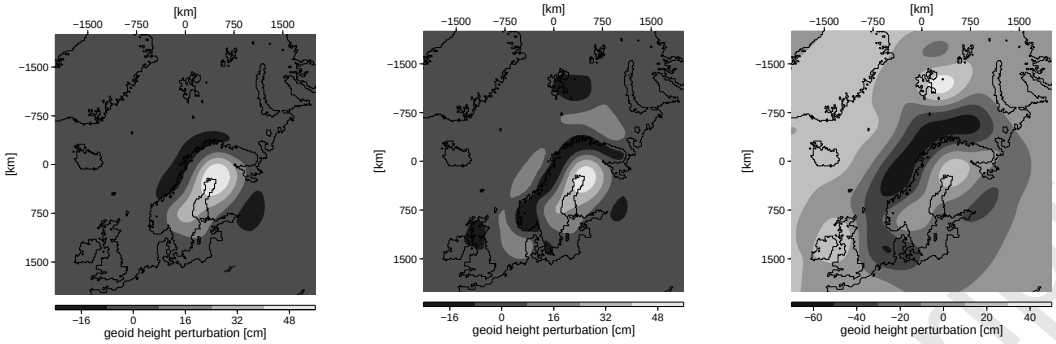


Fig. 14. Geoid height perturbations due to a laterally heterogeneous $LT$ in the absence of an LVZ **(a)**, and combined effect of a laterally heterogeneous $LT$ and CLVZ **(b)** or ALVZ **(c)**

**(a)** background, error in geoid heights

**(b)** CLVZ, error in geoid height pert.

**(c)** ALVZ, error in geoid height pert.

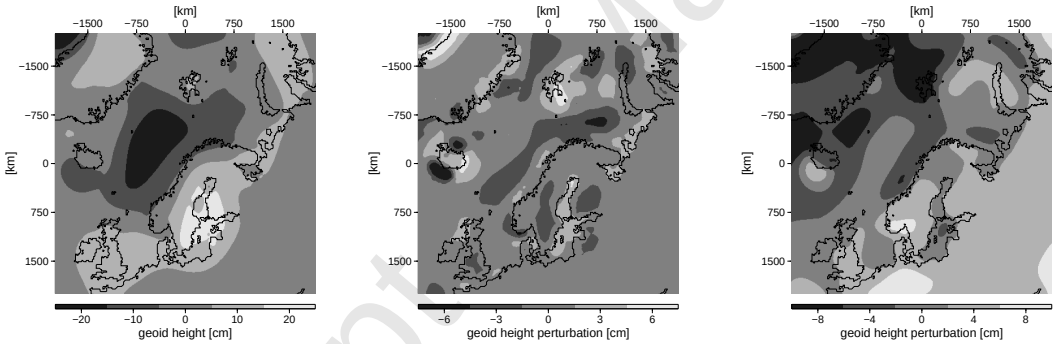


Fig. 15. Errors introduced by using a eustatic ocean load in geoid heights for the background model **(a)**, and in geoid height perturbations for a CLVZ **(b)** and ALVZ **(c)**

Table 1

Radial earth stratification in which the lower crust and the asthenosphere can have an LVZ of $10^{19}$ Pas

| Layer | Depth [km] | Density $\rho$ [kg/m3] | Rigidity $\nu$ [GPa] | Viscosity $\eta$ [Pas] |
|---|---|---|---|---|
| upper crust | 0 | 2700 | 27 | elastic |
| lower crust | 20 | : | : | elastic or $\mathbf{10^{19}}$ |
| lithosphere | 30 | 3380 | 68 | elastic |
| asthenosphere | 80 | : | : | $10^{21}$ or $\mathbf{10^{19}}$ |
| low-velocity zone | 140 | : | : | $10^{21}$ |
| upper mantle | 220 | 3480 | 77 | : |
| transition zone | 400 | 3870 | 108 | : |
| lower mantle | 670 | 4890 | 221 | $10^{21}$ |
| core | 2891 | 10925 | 0 | 0 |

Table 2

Error estimates for the use of a regional model in a global background model. GEO are geoid heights and VEL are horizontal velocities, L indicates that the error has a long-wavelength (>∼ 1000 km) signature and S a short-wavelength (<∼ 1000 km).

| Source | Quantity | total | CLVZ pert. | ALVZ pert. |
|---|---|---|---|---|
| FE vs. SP | GEO | 1% (L) | 5% (S [a]) | 10% (S [a]) + 10% (L) |
| | VEL | 50% (L) | 5% (L [b]) | 25% (L [b]) |
| EU vs. RO | GEO | 1% (L) | 25% (S [c]) | 10% (L) |

[a] can probably be removed using smaller gridsize or quadratic elements (Section 4)

[b] can probably be reduced by increasing the horizontal extent of the FE model (Section 4)

[c] can be somewhat reduced using the RO instead of the EU load output of the SP model (Section 6)